

Phase-resolved X-ray spectroscopy of the millisecond pulsar SAX J1808.4–3658

Marek Gierliński^{1,2}, Chris Done¹, Didier Barret³

¹Department of Physics, University of Durham, South Road, Durham DH1 3LE, UK

²Astronomical Observatory, Jagiellonian University, Orla 171, 30-244 Kraków, Poland

³CESR, 9 avenue du Colonel Roche, BP 4346-31028, Toulouse, Cedex 4, France

Submitted to MNRAS

ABSTRACT

We present new results based on *RXTE* observations of the millisecond pulsar SAX J1808.4–3658 carried out during the decay of the April 1998 outburst. The X-ray spectrum can be fitted by a two-component model. We interpret the soft component as blackbody emission from a heated spot on the neutron star, and the hard component as coming from Comptonization in plasma heated by the accretion shock as the material collimated by the magnetic field impacts onto the neutron star surface. The hotspot is probably the source of seed photons for Comptonization. The hard component illuminates the disc, giving rise to a reflected spectrum. The amount of reflection indicates that the disc is truncated at fairly large radii ($20\text{--}40 R_g$), consistent with the lack of relativistic smearing of the spectral features. The inferred evolution of the inner radius is not consistent with the magnetic field truncating the disc. Instead it seems more likely that the inner disc radius is set by some much longer time-scale process, most probably connected to the overall evolution of the accretion disc. This disc truncation mechanism would then have to be generic in all low mass accretion rate flows both in disc accreting neutron stars and black hole systems.

The phase resolved spectra show clearly that the blackbody and hard Comptonized spectra pulse independently. This obviously gives an energy dependent phase lag. Full general relativistic effects are not required to explain this. The soft blackbody component is optically thick, so its variability is dominated by its changing projected area, while the Doppler shifts (which are maximized 90° before the maximum in projected area) are somewhat stronger for the translucent column.

We do not detect Compton reflection from the neutron star surface, though we predict that it should be present in the X-ray spectrum. This would give an unambiguous observational measure of M/R if there is any iron on the neutron star surface which is not completely ionized.

Key words: accretion, accretion discs – pulsars: individual (SAX J1808.4–3658) – X-rays: binaries

1 INTRODUCTION

Neutron stars and Galactic black holes have very similar gravitational potentials, so the accretion flow in these systems might also be expected to be similar. The key difference is that neutron stars have a solid surface. Therefore, they can have a boundary layer and thermal emission from the surface. Additionally, where there is a strong magnetic field the accretion flow is collimated along the field lines. When the spin and magnetic axes are misaligned the surface emission should be coherently pulsed at the spin period. This is seen in the X-ray pulsars – high mass X-ray binary systems where

young, rapidly rotating neutron stars with a high magnetic field ($\geq 10^{12}$ G) collimate the accreting material onto the magnetic poles. However, up till 1998 no *millisecond* pulses were seen from the low mass X-ray binaries (LMXBs), so there was no direct measure of the spin and magnetic field in such systems. This would be an important test of models of the formation of the millisecond pulsars. Currently the most probable scenario for these rapidly rotating, low magnetic field ($\sim 10^8$ G) neutron stars is that their progenitors are the LMXBs, where the neutron star is spun up through accretion torques, which also might dissipate the magnetic field (e.g. the review by Bhattacharya & Srinivasan 1995).

This situation changed dramatically with the discovery of the coherent X-ray pulsations with 2.5 ms period from the transient X-ray source SAX J1808.4–3658 (Wijnands & van der Klis 1998a). Its rapid rotation and inferred magnetic field of a few $\sim 10^8$ G is in excellent agreement with the predictions of the millisecond pulsar progenitor models (Psaltis & Chakrabarty 1999). The key question is then what makes SAX J1808.4–3658 so different from the rest of the LMXBs? There are only a rather limited number of fundamental parameters which determine the accretion flow – the mass of the neutron star, mass accretion rate, magnetic field, spin of the neutron star and angle between the spin and magnetic axes. These could be coupled with the age and/or evolutionary state of the system, and a further variable which could alter the appearance of the system is its inclination angle to the line of sight.

One way in which to look for differences is to do a detailed comparison of the spectrum and variability of SAX J1808.4–3658 with other neutron star LMXBs. These fall into two main categories, atolls and Z sources, named after their different behaviours on a colour–colour diagram (Hasinger & van der Klis 1989). Atolls can show rather hard spectra dominated by a power law component, similar to that seen in the galactic black holes (e.g. Mitsuda et al. 1989; Yoshida et al. 1993; Barret et al. 2000). This hard or island state is generally seen only at mass accretion rates below a few per cent of Eddington (Ford et al. 2000). Above this the source spectrum makes a rapid transition to a much softer spectrum, termed the banana branch, so tracing out a C (or atoll) shape on a colour–colour diagram. Conversely the Z sources move from a horizontal branch, through a normal branch to the flaring branch as their mass accretion rate increases, tracing out a Z shape on a colour–colour diagram. The power spectral properties also correlate with atoll or Z source classification, and with position on the colour–colour diagram (see e.g. the review by van der Klis 1995).

The broad band spectrum of SAX J1808.4–3658 is entirely typical of an atoll system in the island state, with a power law hard X-ray spectrum (Heindl & Smith 1998; Gilfanov et al. 1998). The variability power spectrum of SAX J1808.4–3658 is also very similar to island state atoll systems (apart from the coherent signal at the spin period): the broad band noise properties (Wijnands & van der Klis 1998b) and even the correlation between the noise break frequency and the QPO frequency matches onto that from other LMXBs (Wijnands & van der Klis 1999).

Thus it seems highly unlikely that there is any large scale difference between the properties of the accretion flow in SAX J1808.4–3658 compared with other neutron star LMXB systems. Yet there is a coherent spin pulse in SAX J1808.4–3658 which is definitely not present in the other atoll systems (Vaughan et al. 1994; Chandler & Rutledge 2000).

There were three observed outbursts of SAX J1808.4–3658: in September 1996 (in 't Zand et al. 1998), in April 1998 (Wijnands & van der Klis 1998a) and in January 2001 (Wijnands et al. 2001). Here we examine the *RXTE* spectra of SAX J1808.4–3658 from 1998 outburst in detail, looking at both the phase averaged and phase resolved spectra at differing mass accretion rates as the outburst declines. We derive a source geometry which is consistent with the obser-

vational constraints, and finally speculate that evolutionary effects are responsible for visibility of the spin pulse.

2 OBSERVATIONS

We analyse *RXTE* observations of 11–29 April 1998 (HEASARC archival number P30411) outburst of the millisecond pulsar SAX J1808.4–3658 using FTOOLS 5.0. We extract the PCA energy spectra from the top layer of detectors 0 and 1 from the Standard-2 data files. A comparison with the Crab spectra shows that a 0.5 per cent systematic error is appropriate in *RXTE* epoch 3 PCA observations for this restricted data selection between energies of 3–20 keV (Wilson & Done 2001). These PCA spectra are combined with the 20–150 keV data from HEXTE cluster 0. The relative normalization of the PCA and HEXTE instruments is still uncertain, so we allow this to be an addition free parameter in all spectral fits. Table 1 contains the log of observations. Observation 1 has a $\sim 12'$ pointing offset, therefore the count rates are lower than in the second observation, though the actual X-ray flux is higher.

We also extract phase-resolved energy spectra from the PCA Event mode data files with timing resolution of 122 μ s (except for the April 13 observation where we used GoodXenon mode files, with resolution of 1 μ s). We have generated folded light-curves in 16 phase bins, for each PCA channel, all layers, detectors 0 and 1. We have chosen beginning of the phase ($\phi = 0$) at the bin with lowest 3–20 keV count rate. Photon arrival times were corrected for orbital movements of the pulsar and the spacecraft. Background files were made from Standard-2 data for exactly the same periods when our phase-resolved spectra were extracted. Power density spectra (PDS) were extracted from the same data files as the phase-resolved spectra, in the 3–20 keV energy range, though we have used all detectors this time. We calculate power density spectra in the $1/128$ –2048 Hz frequency range from averaging fast Fourier transforms over 128 s data intervals.

All spectral analysis (both phase-resolved and phase-averaged) is done using the XSPEC 11 spectral package (Arnaud 1996). The error of each model parameter is given for a 90 per cent confidence interval. We fix the absorption to the interstellar Galactic one in the direction of SAX J1808.4–3658 of 1.3×10^{21} cm $^{-2}$, and use photoelectric cross-sections of Morrison & McCammon (1983).

There is no good determination of the inclination of the system. Lack of X-ray eclipses yields the upper limit of the inclination angle, $i < 81^\circ$. On the other hand modelling of the optical companion's multi-band photometry with a simple X-ray heated disc model suggests $i > 63^\circ$ (Bildsten & Chakrabarty 2001). For reflection models we simply fix $i = 60^\circ$, a value which we will show to be consistent with other source properties later on. We assume solar abundances of the reflector. To convert fluxes to luminosity we use the distance to the source of 2.5 kpc (in 't Zand et al. 2001).

3 RESULTS

Table 1. Log of *RXTE* observations. Start and end times are in the UT days of April 1998. Exposures are in seconds and count rates are in counts per second from layer 1 of detectors 0 and 1 (PCA) and from cluster 0 (HEXTE). The count rate of the first observation is lower due to $\sim 12'$ source offset.

No.	Obsid	Start	End	PCA		HEXTE	
				Exposure	Count rate	Exposure	Count rate
1	30411-01-01-03S	11.809	11.905	1968	256.5 ± 0.5	1065	11.2 ± 0.5
2	30411-01-02-04S	13.078	13.100	1312	296.4 ± 3.2	449	16.4 ± 0.8
3	30411-01-03-00	16.721	17.194	14032	182.4 ± 0.2	4483	10.7 ± 0.2
	30411-01-04-00						
4	30411-01-05-00	18.131	18.388	14320	157.2 ± 0.2	4549	9.1 ± 0.2
5	30411-01-06-00	18.860	19.044	7296	149.4 ± 0.2	2481	7.9 ± 0.3
6	30411-01-07-00	20.877	20.964	4224	124.8 ± 0.2	1451	6.7 ± 0.4
7	30411-01-08-00	23.662	23.973	14512	105.4 ± 0.2	4726	5.3 ± 0.2
8	30411-01-09-01	24.672	24.974	14160	101.3 ± 0.2	4708	5.3 ± 0.2
	30411-01-09-02						
9	30411-01-09-03	25.599	25.904	14352	96.4 ± 0.1	4724	5.3 ± 0.2
	30411-01-09-04						
10	30411-01-09-00	26.668	26.978	15456	63.9 ± 0.1	5068	3.2 ± 0.2
11	30411-01-10-01	27.604	27.814	8896	33.5 ± 0.1	2914	2.1 ± 0.3
	30411-01-10-02						
12	30411-01-10-00	29.600	29.790	8512	26.5 ± 0.1	2303	2.2 ± 0.3

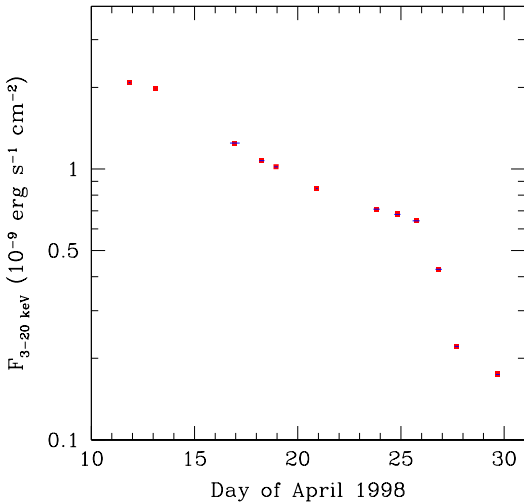


Figure 1. Outburst of SAX J1808.4-3658: 3-20 keV unabsorbed flux of observations 1-12 (Table 1).

3.1 Outburst light-curve

The 3-20 keV flux evolution after the outburst is presented in Fig. 1 (see also Cui, Morgan & Titarchuk 1998; Gilfanov et al. 1998). During about 20 days after the outburst the flux declined by about factor ten. The bolometric unabsorbed flux (obtained using the model described below in Section 3.2) at the maximum is 5.1×10^{-9} erg cm $^{-2}$ s $^{-1}$ which corresponds to bolometric luminosity of about 3.8×10^{36} erg s $^{-1}$, which is 2.2 per cent of Eddington luminosity. The outburst follows a roughly exponential decay, with a sudden drop in the lightcurve around 26th of April.

3.2 Phase-averaged energy spectra

We select observation 3 with the best statistics for spectral fits. We model this first with a power-law and exponential cutoff but the fit is very poor, with $\chi^2 = 351$ for 82 degrees of freedom. There are significant residuals in the PCA above ~ 7 keV. We model these as Compton reflection using angle-dependent Green's functions of Magdziarz & Zdziarski (1995) and a narrow Gaussian representing iron K α fluorescent line. The reflected spectrum is determined by the solid angle subtended by the reflector, Ω , inclination angle i , and ionization parameter $\xi \equiv 4\pi F_{\text{ion}}/n$ (where F_{ion} is the 0.005-20 keV irradiating flux in a power-law spectrum and n is the density of the reflector). We allow for relativistic smearing of the reflected component and the line for a given inner disc radius, R_{in} . The fit is much better now, $\chi^2 = 101/78$, but there is still a strong excess below ~ 5 keV. Including a blackbody soft component finally gives a good fit, with $\chi^2 = 70.6/77$. Parameters for this best fit phenomenological model are given in Table 2.

We replace the phenomenological model above with a more physically motivated description of the spectrum. Instead of the power law we use an approximate solution of the Kompaneets (1956) equation (Zdziarski, Johnson & Magdziarz 1996) to model the thermal Comptonization hard component in the spectrum. The model `thcomp` is parameterized by the asymptotic power-law photon index, Γ , electron temperature, T_e and blackbody seed photons temperature, T_{seed} . Though the seed photons temperature *can* be independent of the soft component temperature, the simplest solution is to equalize them. Later on we will argue that indeed the observed blackbody is the source of seed photons. We calculate the reflected spectrum from this continuum using a more sophisticated reflection model where both the continuum reflection and the line are calculated self-consistently for a given ionization state (Życki, Done & Smith 1998). The reflected spectrum (continuum and line) is relativistically smeared for a given inner disc radius, R_{in} .

Table 2. Best-fitting parameters of the power law plus blackbody and reflection model fitted to the data set 3. The reflector inclination was 60° , and we assumed solar abundances. ξ and R_{in} were frozen, while computing the parameter errors.

Parameter	Value
kT_{soft} (keV)	0.77 ± 0.03
N_{soft} (km 2)	10.6 ± 1.9
Γ	1.82 ± 0.04
E_f (keV)	180^{+120}_{-60}
$\Omega/2\pi$	0.05 ± 0.04
ξ (erg cm s $^{-1}$)	1900
$R_{\text{in}}(R_g)$	30
E_{line} (keV)	6.5 ± 0.15
EW_{line} (eV)	85 ± 20
χ^2	70.6/77 d.o.f.

For the soft component we use a single-temperature blackbody. Again, the inclusion of the soft component is *required* by the data: using just a Comptonization model and its reflection gives $\chi^2 = 174/79$. Allowing the absorption to be free reduces this only to $\chi^2 = 166/78$, whereas with a blackbody the fit is $\chi^2 = 73.6/80$. The same is if we use more conservative 1 per cent systematic errors in the PCA spectra instead of 0.5 per cent. A fit without the soft component gives $\chi^2 = 130/79$ while adding a blackbody reduces χ^2 to 58.2/80. The lack of data below 3 keV in the PCA means that we see only the high-energy part of the soft component, so its overall spectral shape is poorly constrained. A multi-colour disc spectrum can equally well fit the soft excess, but we choose to use a blackbody as its variability implies that it arises from a hot spot on the neutron star surface (see section 3.4).

Due to poor statistics, the electron temperature is poorly constrained by the HEXTE data, particularly for later observations when the source is fainter. From the fits we obtain lower limits on kT_e only, typically ≥ 30 keV. Similarly, the reflector ionisation state and amount of relativistic smearing are also poorly constrained. To get the maximum possible signal-to-noise we co-add observations 3–12 and fit this total spectrum. This gives an electron temperature of $kT_e = 90^{+240}_{-30}$ keV. The reflector ionisation state is $\xi = 1000^{+2100}_{-800}$ erg cm s $^{-1}$, and there is still only an upper limit on the amount of relativistic smearing. Hereafter we fix the electron temperature and disk ionisation at these best fit values, and fix the inner disc radius at $50R_g$ (where $R_g \equiv GM/c^2$).

We fit all the phase averaged spectra using this model consisting of the thermal Comptonization, Compton reflection and the blackbody. Fit results are presented in Fig. 3, and an example of the spectral decomposition is shown in Fig. 2.

Despite an order of magnitude change in the observed flux during the declining part of the outburst, the energy spectrum did not change very much (see Gilfanov et al. 1998). There is a slight softening in the hard component, starting from 24th April onwards. The amount of reflection is always low, $\Omega/2\pi \sim 0.08$, except for the first observation, where it was about a factor of 2 times higher. The soft component decreased both its temperature and apparent area,

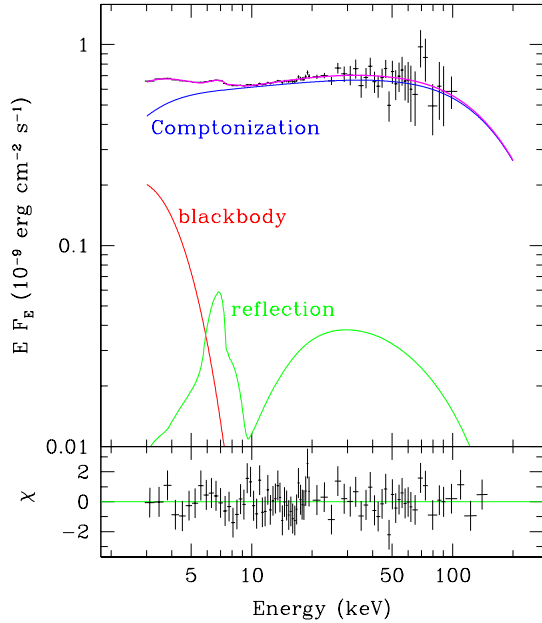


Figure 2. Phase-averaged energy spectrum of SAX J1808.4-3658 (observation 3) with a model consisting of a thermal Comptonization, blackbody and Compton reflection.

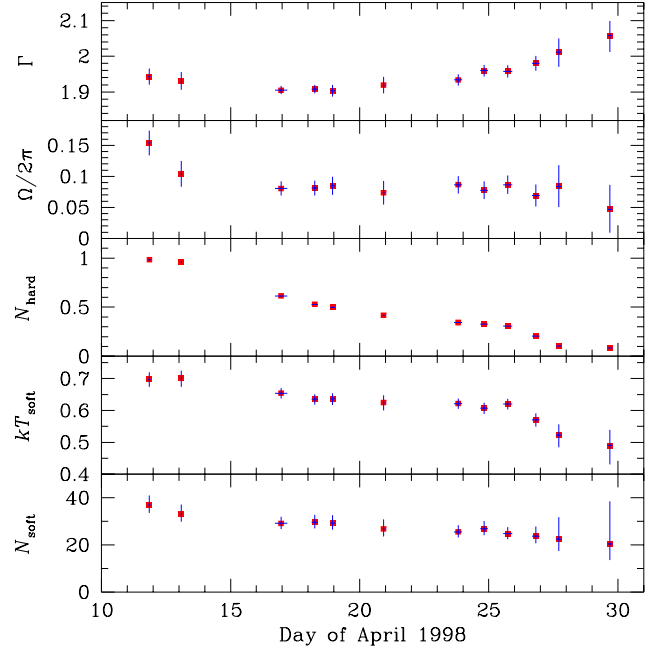


Figure 3. Fit results of the blackbody plus thermal Comptonization and reflection model to the phase-averaged spectra of observations 1–12. Γ is the asymptotic power-law photon index, Ω is the solid angle subtended by the reflector, N_{hard} (10^{-9} erg cm $^{-2}$ s $^{-1}$) is the normalization of the hard (Comptonization) component at 10 keV, kT_{soft} (keV) and N_{soft} (km 2) are the temperature and apparent area of the soft (blackbody) component, respectively.

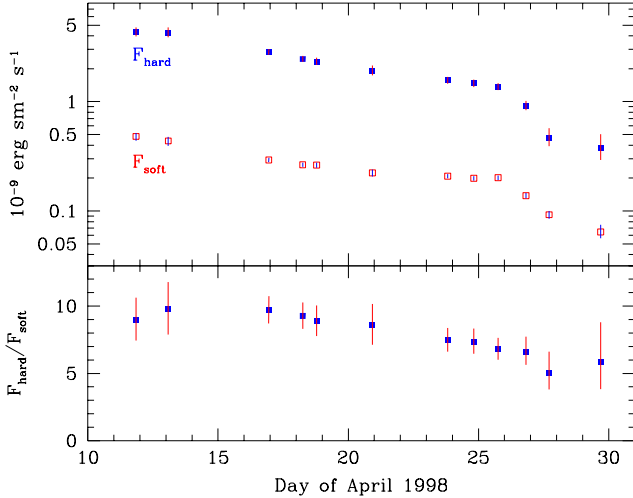


Figure 4. Bolometric fluxes from the best-fitting model of the hard and soft components.

though this did not affect the overall spectral shape very much.

We use the unabsorbed best-fitting model (without reflection) to compute the bolometric fluxes from the hard and soft components (Fig. 4). The ratio of $F_{\text{hard}}/F_{\text{soft}}$ decreased roughly by factor two, though the errors of measurement are substantial and, to some extent, model dependent. It is however clear that the evolution of F_{soft} closely followed that of F_{hard} . Thus, both components must be closely linked in some way.

The Comptonization model we use here is only an analytical approximation. Therefore, we check it's validity and how it affects our fitting results, using `CompPS` Comptonization code (Poutanen & Svensson 1996), which finds a numerical solution of the Comptonization problem explicitly considering successive scattering orders. We fit the co-added spectrum assuming that the Comptonizing cloud has a shape of a cylinder with height-to-radius ratio $H/R = 1$ and the seed photons come from the bottom. We find the best-fitting electron temperature $kT_e = 43^{+9}_{-6}$ keV and vertical optical depth of the cylinder of $\tau = 2.7^{+0.3}_{-0.4}$. While the Compton parameters change, the spectral shape is very similar, and the inferred soft excess is almost identical (blackbody parameters of $kT_{\text{soft}} = 0.65 \pm 0.02$ keV and $N_{\text{soft}} = 29 \pm 3$ km^2 with `thcomp` compared to $kT_{\text{soft}} = 0.68 \pm 0.02$ keV and $N_{\text{soft}} = 33 \pm 3$ km^2 for `compPS`). Therefore, we conclude that the detailed choice of the Comptonization model does not affect the fit results of the soft component.

We have assumed solar abundances of the reflector, though we expect the companion star to be highly evolved and helium rich (see e.g. Ergma & Antipova 1999). However, the shape of the reflected spectrum in X-rays is determined mostly by heavy elements, so variation in the abundance of hydrogen and helium would affect the reflected spectrum only very little (e.g. George & Fabian 1991). Additionally, the amount of reflection is rather small, so the effect of abundances on the total spectrum is even weaker. The spectral resolution and response uncertainties of the PCA do not allow us to investigate this issue in detail.

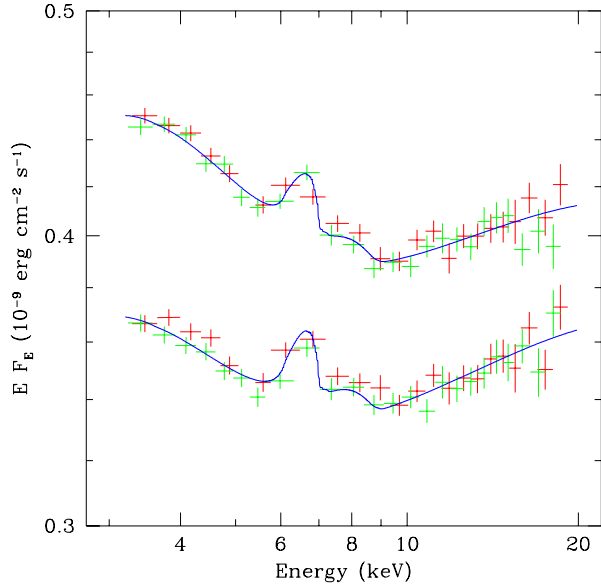


Figure 5. Phase-resolved spectra with lowest and highest N_{hard} , corresponding to phase 0 and 0.44, respectively. The vertical axis is blown-up here to enhance the features of the spectra.

Next, we check for the presence of the Compton reflection from the neutron star surface. Depending on the equation of state we should expect this reflection to be redshifted by $z = 0.07\text{--}0.77$ (Miller, Lamb & Psaltis 1998). This means that the most prominent reflection features, the iron K line and edge, can appear between 3.6 and 6.0 keV. Unfortunately, this coincides with the PCA instrumental Xenon edge at 4.8 keV, therefore the following results should be treated with caution. We add another reflection component in our model with redshift allowed to be free between the above limits and fit the data. If the neutron star surface is fairly highly ionized, with $\xi = 1000 \text{ erg cm s}^{-1}$, we find an upper limit for $\Omega_*/2\pi < 0.012$ for a redshift range of $z = 0.07\text{--}0.77$. However, if the neutron star surface is completely ionized, the reflected spectrum is simply a featureless power law with high-energy cutoff around 30 keV and the same spectral index as irradiating Comptonization. In such a case we cannot disentangle the irradiating and reflected continuum, so there are no constraints on the amplitude of the reflection from the neutron star.

3.3 Phase-resolved energy spectra

The phase-resolved spectra with the lowest and highest flux are shown in Fig. 5. There is a slight softening of the highest flux spectrum at energies below ~ 5 keV, but otherwise the spectral shape is remarkably constant. To investigate the details of spectral evolution with the pulse phase we fit the phase-resolved spectra by the blackbody plus thermal Comptonization model (`thcomp`), the same we used in Section 3.2 to fit the phase-averaged spectra. We fit each spectrum of the 16 phase bins and find the fit parameters and their errors. The results are presented in Fig. 6, with an average $\chi^2_\nu = 45.9/44$ per spectrum.

We clearly see that some parameters vary more than the

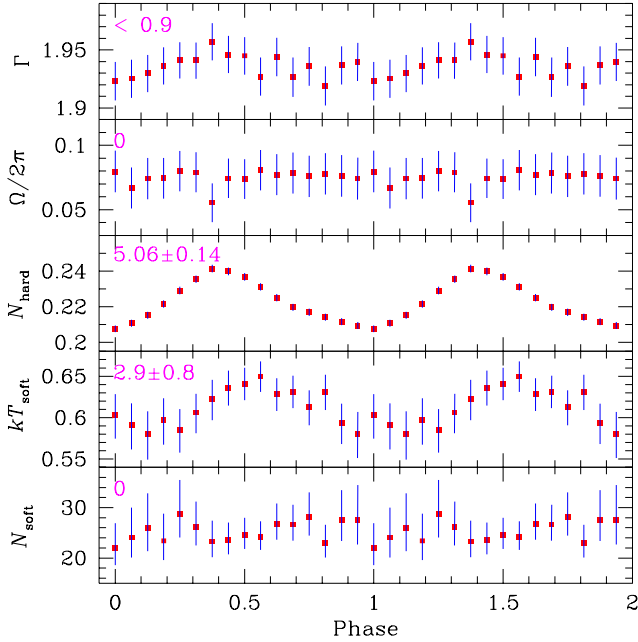


Figure 6. Fit results of the blackbody plus thermal Comptonization and reflection model fitted to the phase-resolved spectra (co-added observations 3–12). Numbers in the panels show the intrinsic variance, S , of the given parameter (per cent). The fit parameters are described in the text and in the caption to the Fig. 3.

others, in particular reflection ($\Omega/2\pi$) is consistent with a constant while N_{hard} exhibits strong sinusoidal pulsations. We want to distinguish between the parameters that vary significantly and those in which variability can be due to statistical noise. Therefore, we quantify the variability of a given parameter by an *intrinsic* variance. Let x_i and σ_i be a given parameter’s best-fitting value and variance, in the i -th phase bin ($i = 1, \dots, N$; here $N = 16$). Then, the intrinsic variance of this parameter is estimated by

$$S = \frac{\sqrt{\langle \sigma^2 \rangle (\chi^2_{\nu} - 1)}}{\langle x \rangle}, \quad (1)$$

where

$$\langle \sigma^2 \rangle \equiv \left(\frac{1}{N} \sum_{i=1}^N \frac{1}{\sigma_i^2} \right)^{-1}. \quad (2)$$

The reduced χ^2_{ν} results from fitting a series of x_i (for $i = 1, \dots, N$) by the constant. When $\chi^2_{\nu} < 1$ we assume $S \equiv 0$. We estimate error of S by propagating data errors,

$$\Delta S \equiv \sqrt{\sum_{i=1}^N \left(\frac{\partial S}{\partial x_i} \right)^2 \sigma_i^2} = \frac{1}{\langle x \rangle} \sqrt{\frac{\langle \sigma^2 \rangle}{N-1} \frac{\chi^2_{\nu}}{\chi^2_{\nu} - 1}}. \quad (3)$$

When S is zero, then any variability is completely consistent with having a statistical origin so that there is no significant intrinsic variability in the parameter. In such a case we decide that the parameter is intrinsically constant, and fix it at its average value for the next series of fits.

Using this we found that only two parameters exhibited significant intrinsic variability: N_{hard} and T_{soft} (see Fig. 6).

We fixed Γ and $\Omega/2\pi$ (but not N_{soft} for a moment) at their average values and refit the spectra (average $\chi^2_{\nu} = 47.3/46$, so a difference of $\Delta\chi^2 = 1.4$ for 2 fewer free parameters). This showed an anti-correlation between the pulse profiles of T_{soft} and N_{soft} , which is most probably a sign of degeneracy in the soft component parameterization. When we additionally fix N_{soft} the average χ^2_{ν} rises only to $48.2/47$, however fixing T_{soft} instead causes significant worsening of the fits with average $\chi^2_{\nu} = 54.1/47$, which means that temperature pulsation is preferred over normalization pulsation. However, from the physical point of view we should expect more variability in apparent area (normalization) than in temperature (see discussion in Section 4.2). We see only Wien part of the blackbody spectrum in the PCA, so there is some degeneracy in the model, namely in the soft component temperature, normalization and the hard component low-energy turnover. This creates model-dependent uncertainty. Therefore, we decide to chose the model with worse χ^2 but better physical foundation, and to fix T_{soft} , letting only the normalizations of the soft and the hard components (N_{hard} and N_{soft}) to be free, and fit the data in each phase bin again. The final result is presented in Fig. 7a.

Thus, we decompose the phase resolved spectra into two independently pulsing components: the soft and the hard one. We fit the pulse profiles of both components by harmonic functions. The N_{hard} pulse profile is clearly asymmetric and cannot be fitted by a single harmonic (we obtain $\chi^2 = 116/13$). However, addition of another harmonic function provides with a very good fit ($\chi^2 = 6.0/11$). Our best-fitting function is

$$N_{\text{hard}}(\phi) = 0.357 + 0.025 \sin[2\pi(\phi - 0.19)] + 0.0044 \sin[2\pi(\phi - 0.24)/0.5] \quad (10^{-9} \text{ergs}^{-1} \text{cm}^{-2}) \quad (4)$$

(where ϕ is the phase). The N_{soft} pulse profile is symmetric and a single harmonic function,

$$N_{\text{soft}}(\phi) = 25.6 + 6.4 \sin[2\pi(\phi - 0.32)] \quad (\text{km}^2), \quad (5)$$

gives a very good fit, $\chi^2 = 3.63/13$. A second harmonic is statistically insignificant, as it improves the fit only by $\Delta\chi^2 = 0.05$, while taking away two degrees of freedom. The upper limit on the second harmonic is 7 per cent of the amplitude of the first one. We show the pulse profiles of both components and the best-fitting functions in Fig. 7.

The pulse profiles of N_{hard} and N_{soft} are shifted in phase in a way that the soft component lags the hard one. This will manifest itself as an energy dependent time lag in which soft X-rays lag hard X-rays, as reported in previous work (Cui et al. 1998). In Fig. 8 we show the time lags taken from Cui et al. (1998) and the prediction of our two-component model in which only the normalizations N_{hard} and N_{soft} are free to vary. Up to about 7 keV, as the contribution from the soft component decreases, the soft time lag quickly increases. Above this energy, where the soft component is negligible, the time lag flattens, and shows the ~ 8 per cent shift in phase (about 200 μ s) between the soft and hard components.

Finally, we use the model with only N_{soft} and N_{hard} free to fit the phase-resolved spectra for each of the observation from 1 to 12. We measure the intrinsic variance of both of the fit parameters, and show the result in Fig. 9. The intrinsic variance of N_{hard} increases monotonically from ~ 4.5 to ~ 6 per cent during the declining part of the outburst. The behaviour of the N_{soft} variance is more complex: it slowly

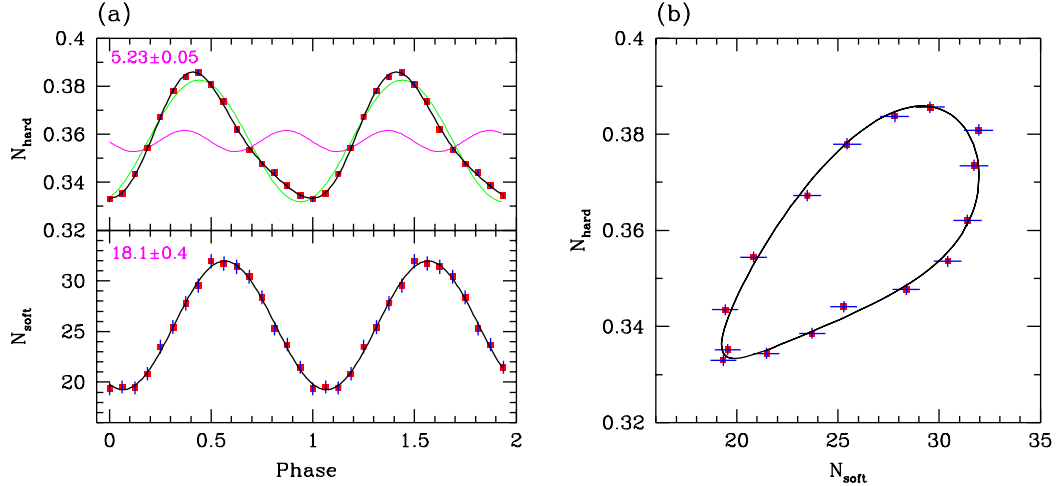


Figure 7. Pulsation of the soft and hard components of the spectrum. The co-added phase-resolved spectra were fitted by the blackbody plus thermal Comptonization and reflection model, where only N_{soft} and N_{hard} were free. See Fig. 6 for the fit with other parameters free. The fit parameters are described in the text and in the caption to the Fig. 3. The models fitted to the pulse-profiles are described in Section 3.3.

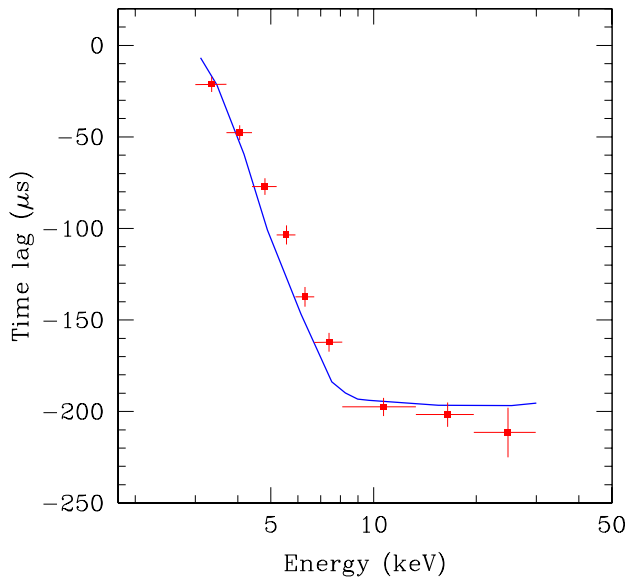


Figure 8. Energy-dependent time lags. The data points were taken from Cui et al. (1998) and the curve represents the prediction of the model with N_{hard} and N_{soft} free.

rises to its maximum around 18 April, then declines only to rise again after 26 April.

Our approach contrasts with that of Ford (2000) in that we use standard background subtraction techniques to extract the phase resolved spectra whereas he used the phase minimum spectrum as the persistent emission and subtracted this from the phase-resolved spectra to get the spectrum of the pulsed component. However, our results clearly show that there are *two* pulsed components, the hard and the soft, and that these *do not* vary in phase. Ford (2000) fit the pulsed emission by a power law, and noticed significant phase variability of the spectral index.

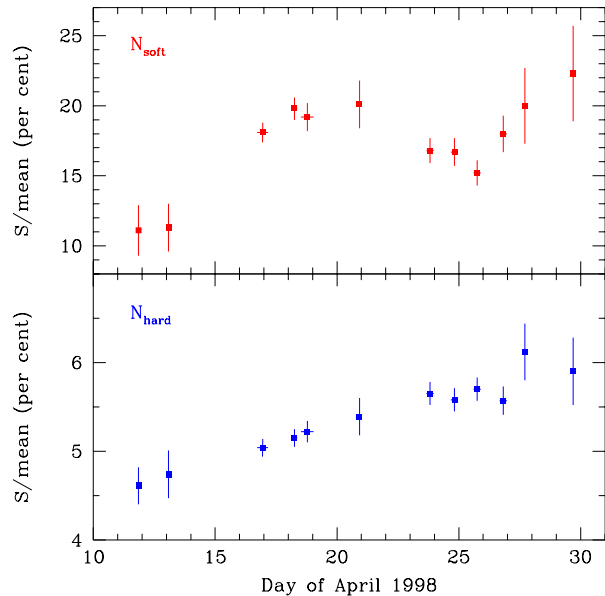


Figure 9. Evolution of intrinsic variance (1) of the two spectral component normalizations, N_{soft} and N_{hard} , when the data is fitted by the blackbody plus Comptonization and reflection model. Other model parameters were fixed during the fits.

However, in this approach a single power law tries to follow the overall spectral shape, which is actually more complex. Additionally, poor statistics of the persistent-emission-subtracted spectra make fitting more difficult. We have reproduced this approach but fitted these pulsed spectra with a model consisting of a power law *and* a blackbody. Interestingly, the power-law index was consistent with remaining constant with phase, while the blackbody and power-law normalizations were shifted in phase, as in our analysis.

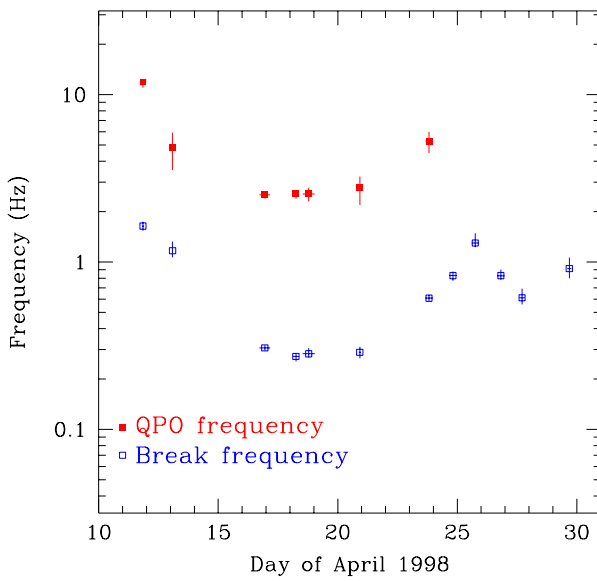


Figure 10. Break and QPO frequencies in the power density spectra.

3.4 Power density spectra

The properties of the power-density spectrum of SAX J1808.4–3658 were described in details by Wijnands & van der Klis (1998b). Here we re-fit the PDS selected from the observations 1–12 (Table 1), using similar model, in order to obtain break and QPO frequencies, corresponding to the exact times at which the data were taken. We show the results in Fig. 10, for completeness.

None of the two frequencies is correlated with the X-ray flux (Fig. 4), with any of the spectral parameters (Fig. 3), nor with spectral colour. While the spectral parameters either remain constant or change monotonically, both break and QPO frequencies reach their minimum around 18 April. After 24 April we do not detect QPO, but the break frequency reverses its rise around 26 April. A similar behaviour (though in opposite direction) can be seen in the soft component variance (Fig. 9). Thus, there is a clear anti-correlation between ν_{break} and $S(N_{\text{soft}})$.

4 DISCUSSION

We now have many interrelated constraints, which can be used to determine the geometry of the system, and how this changes as the outburst declines. Since both hard and soft X-rays pulsate then they must be affected by the spin of the neutron star. We assume that the underlying geometry involves a hotspot on the surface of the neutron star to produce the soft pulsed component, and a hard X-ray shock above the magnetic poles to produce the pulsed hard X-ray component. The constancy of the hard X-ray spectral shape with spin phase implies that the hard X-rays are from a single type of emission region, rather than being the sum of a pulsed and unpulsed component. The sinusoidal light-curve for the soft component as a function of spin phase strongly implies that we see only one hotspot. The shape of the hard

component light-curve probably implies that we don't see the second shock.

More constraints come from the variability characteristics. It is commonly accepted that the QPO frequency is related to the inner disc radius in some way. The inner disc radius, together with the shock height and the neutron star radius, determines the solid angle subtended by the disc, and so the amount of reflection and seed photons from the disc. Seed photons can also arise from the hotspot on neutron star surface, and their contribution is determined mostly by the shock height. But the spectral shape gives us observational constraints on the amount of reflection from the disc, and the amount of the seed photons, so there should be a unique solution to the geometry of the system. In practice of course, there are significant observational and theoretical uncertainties, but we use these observational constraints to develop a consistent geometrical picture for the emission from SAX J1808.4–3658.

4.1 Emission mechanisms

The 3–200 keV spectrum *requires* a two component model. The soft component is consistent with a blackbody at ~ 0.5 – 0.7 keV. The hard component can be described by thermal Comptonization of these blackbody seed photons in plasma of optical depth of ~ 2 and temperature of ~ 40 keV. The soft and hard component fluxes are very closely correlated (see Fig. 4). Thus the soft component is most probably from reprocessing of the hard component. We further discuss relation between both components in Appendix B.

4.2 Hotspot

We consider the source of the soft component as a simple circular hotspot on the surface of the neutron star. We take into account Doppler shifts and geometry in the rotating system of the neutron star. We demonstrate, how in the frame of this simple model the data can constrain inclination angle of the system and the size of the hotspot.

The pulse profile of the soft component is consistent with a single sinusoid. This implies that we *do not* see the second spot, since it would have given rise to a secondary maximum in the profile. This, in turn, yields a constrain on the spot radius,

$$\frac{R_{\text{spot}}}{R_*} < \frac{\pi}{2} - i - \delta, \quad (6)$$

where i is the inclination angle of the observer from the rotation axis, δ is the angle from the rotation axis to the spot at the magnetic pole and R_* is the neutron star radius.

The inferred luminosity of a spot depends on both its temperature and projected area. Both of these change as a function of phase. The Doppler shift gives a ratio between the maximum and minimum temperature of

$$\frac{T_{\text{max}}}{T_{\text{min}}} \sim \frac{1 + \beta_{\text{eq}} \sin \delta \sin i}{1 - \beta_{\text{eq}} \sin \delta \sin i}, \quad (7)$$

where $\beta_{\text{eq}} \equiv v_{\text{eq}}/c \sim 0.08$ is the equatorial rotation speed of the neutron star. The ratio of $T_{\text{max}}/T_{\text{min}}$ is only weakly affected by the spot size. The maximum-to-minimum ratio of the projected area is

$$\frac{A_{\max}}{A_{\min}} = \frac{\cos(i - \delta)}{\cos(i + \delta)}, \quad (8)$$

where the maximum area is offset in phase by 90° from the maximum Doppler shift. This formula is exact even for a large circular spot, again assuming that we do not see the spot from the second pole.

When the temperature of the soft component is a free parameter in the fits to the phase-resolved spectra (Section 3.3) then it yields large modulation in this temperature, with $T_{\max}/T_{\min} = 1.12$ (see Fig. 6). However, physically we expect a rather small variation in temperature from the Doppler shift, since the offset angle between the magnetic spin and the rotation axis is probably small (Ruderman 1991). Assuming an inclination angle of $i = 60^\circ$ and offset angle of $\delta = 10^\circ$ we find $T_{\max}/T_{\min} = 1.02$, much less than observed. Furthermore, this would give an inferred luminosity modulation of about 1.08, much less than the observed minimum-to-maximum ratio of 1.7. Therefore, Doppler effects alone are *unlikely* to be the predominant cause of the variability, contrary to Ford (2000).

Conversely, for these parameters the projected area variability results in a maximum-to-minimum luminosity ratio of 1.9. Thus it seems likely that the majority of the luminosity change should come from the change in projected area while the temperature remains mostly constant.

To check consistency of these predictions with the data, we fit the phase-resolved spectra leaving only N_{hard} and N_{soft} as free parameters, but additionally enforcing sinusoidal variation of T_{soft} with maximum-to-minimum ratio of 1.02, as predicted using Equation (7). As a result, maximum-to-minimum ratio of N_{soft} is 1.56. We use these numbers to constrain the inclination and offset angles. We solve Equation (8) with $A_{\max}/A_{\min} = 1.56$. This gives us one-to-one relation between i and δ (Fig. 11a). For the inclination angle of $i = 60^\circ$ the corresponding offset is $\delta = 7^\circ$. Equations (6) and (8) then give an upper limit for the hotspot radius (Fig. 11b). We find $R_{\text{spot}} < 0.4R_*$, or $R_{\text{spot}} < 4$ km, assuming $R_* = 10$ km.

The hotspot emission gives us an independent way to estimate its size. From the blackbody normalization we estimate its average projected area as $\sim 30 \text{ km}^2$ (see Fig. 3). This is a lower limit as some of the hotspot could be obscured by the shock, and we have not included gravitational redshift. Nonetheless, for an inclination of 60° this yields $R_{\text{spot}} \gtrsim 4$ km. Given that we then have both an upper and lower limit for the spot size of ~ 4 km, we take this as our estimate of the spot size.

For the maximum possible inclination angle of $i = 80^\circ$ the required offset is small, $\delta = 2^\circ$. This yields in turn $R_{\text{spot}} < 0.1R_*$, which is not consistent with our lower limit on the hotspot size from the normalization of the blackbody. Therefore, we find the inclination angle of $i = 60^\circ$ the most likely.

Our discussion neglects general relativistic effects. These will change the quantitative results, but for our model then the effects of light bending are not particularly strong. Full relativistic calculations by Psaltis, Özel & DeDeo (2000) show that the inferred area of the spot is within 10 per cent of its intrinsic area for our model geometry, where the spot is large and not eclipsed. Thus the qualitative constraints derived here on the geometry should be valid.

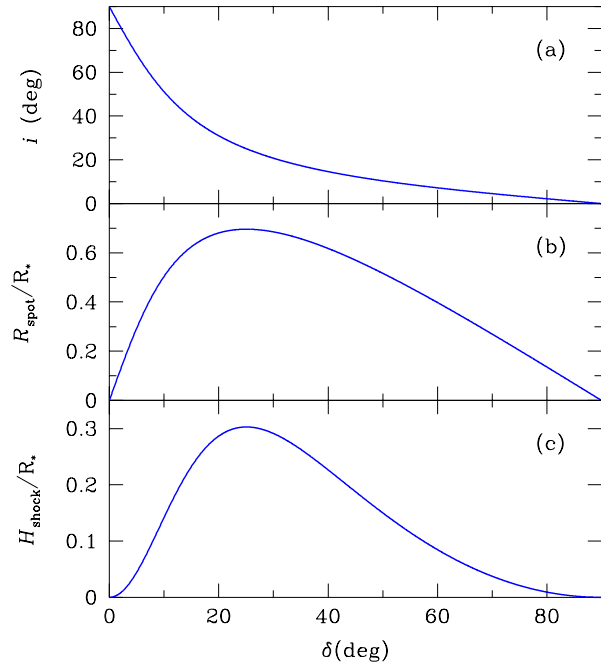


Figure 11. (a) Solution of the Equation (8), assuming maximum-to-minimum area amplitude of the soft component $A_{\max}/A_{\min} = 1.52$. (b) The upper limit on the radius of the hotspot, from Equations (6) and (8). (c) The upper limit on the shock height from Equations (9) and (8).

4.3 Shock

We consider the source of the hard component as an X-ray emitting shock in the accretion column. We again take into account Doppler shifts and geometry.

The hard component pulse profile, like the soft one, lacks the secondary maximum, which implies that we *do not* see the second shock. This immediately yields strong constraints on the shock height:

$$\frac{H_{\text{shock}}}{R_*} < \frac{1}{\sin(i + \delta)} - 1. \quad (9)$$

The solution to this equation, solved simultaneously with the offset-inclination relation (8) derived above is shown in Fig. 11c. For a small offset angle of $\delta = 7^\circ$ the shock must be short, $H_{\text{shock}} < 0.1R_*$.

The hard X-ray spectrum can be described as a power law with photon spectral index $\Gamma \approx 2$. We can expect it to be almost isotropic. Then, in the non-relativistic limit the Doppler shift gives the ratio of maximum-to-minimum observed hard flux, as

$$\frac{F_{\max}}{F_{\min}} = \left(\frac{1 - \beta_{\text{eq}} \sin i \sin \delta}{1 + \beta_{\text{eq}} \sin i \sin \delta} \right)^{-2-\Gamma}. \quad (10)$$

For $\delta = 7^\circ$ and $i = 60^\circ$ this ratio is 1.07, while the observed maximum-to-minimum is 1.16. An additional source of variability could be reflection from the neutron star surface and/or anisotropy of the shock emission. The reflection from the fully ionized surface would be spectrally indistinguishable from the irradiating continuum and so is consistent with our spectral fits (see Appendix C). For the above

inclination and offset angles the reflection component should have maximum-to-minimum flux ratio of about 1.2.

Unlike the soft component pulse profile, the hard one is not symmetric: it is skewed. In Section 3.3 we have fitted this profile with two sinusoids: a dominating one with the spin frequency and a weaker one, with double-spin frequency. This can be explained if the cross-section of the shock is elongated, with bi-axial symmetry, which would create a double-spin frequency on top of the main, single-spin frequency pulse profile. In reality, magnetic-field induced column accretion onto the neutron star surface might create a latitudinal-elongated, crescent-shaped shock cross-section.

4.4 Phase shift

There are two main sources of phase-dependent variability: Doppler shifts and variation in the projected area. As the spot goes around the spin pole, the projected area is maximized when the spot is closest to the observer, while the Doppler shifts are maximized when the spot is midway between its closest and furthest points, as this is where its velocity along the line of sight is largest.

Both Doppler and projected area effects should affect the source spectrum. However, the spin pulse variability of the soft component is probably dominated by the projected area terms (see Section 4.2). If the hard component were dominated by Doppler shift then the two components should be shifted in phase by 90° . However, should be some projected area effects in the hard emission, both from observing the translucent column at differing angles and from the presence of highly ionized reflected continuum emission (see Section 4.3). This means that the hard spectrum varies as the weighted sum of these components, one which peaks as the Doppler emission and one which peaks as the effective area. Thus the maximum of the hard emission moves closer to the soft emission. While detailed modelling depends on the unknown geometry of the accretion column, it seems possible that this can result in the observed phase lag of $\sim 50^\circ$ (Fig. 7).

This is a very different interpretation to the observed energy dependent phase lag than that of Ford (2000). Ford (2000) used only a single blackbody component at $kT \sim 0.6$ keV as the pulsing spectrum. This does give energy dependent phase lags, but of course contributes very little to the hard spectrum. Although he does get 10 per cent variability at 20 keV, this is measured with respect to the blackbody rather than to the total spectrum. Since the blackbody flux contributes only a tiny fraction (5×10^{-9}) of the total flux at 20 keV, his 10 per cent variation of the blackbody flux predicts only a 5×10^{-8} per cent modulation at 20 keV, so cannot explain the observed phase lags in the total spectrum. By contrast, our model can explain the observed time lags, as shown in Fig. 8. In particular, it predicts flattening of the time lag above ~ 7 keV, where the soft component is negligible. The key assumption required by our model is its two-component nature. There is the soft and hard spectral component and they pulsate *shifted in phase*. Whatever is the actual geometry, this phase shift is required to see the time lags.

4.5 Long Term variability

The 2–50 keV luminosity of SAX J1808.3–3658 changed by an order of magnitude during the decline from outburst, yet the spectral shape remained remarkably constant. However, neutron star binaries in general show a dramatic transition from hard-to-soft at a 2–50 keV luminosity ~ 0.01 of L_{Edd} (Ford et al. 2000), corresponding to a bolometric luminosity of a few per cent of Eddington. This spectral switch is startlingly like that seen in GBHC at low bolometric luminosities (e.g. Nowak 1995). This similarity makes it likely that the underlying mechanism for the transition is the same irrespective of the nature of the compact object, so implying a connection to the accretion flow itself rather than to anything to do with a magnetosphere or solid surface.

Assuming the distance of 2.5 kpc (in 't Zand et al. 2001) the 2–50 keV flux during the outburst changed from 0.01 to 0.001 of L_{Edd} (where $L_{\text{Edd}} = 2.5 \times 10^{38}$ erg s $^{-1}$), so it is likely that SAX J1808.3–3658 never became quite bright enough to change from the hard (island) state to the soft (banana) state. The reason for the low peak outburst luminosity is easy to find. The binary is a very small system with an orbital period of only 2.1 hours (Chakrabarty & Morgan 1998), so the disc outer radius (set by tidal truncation) is also small ($R_{\text{out}} \sim 2 \times 10^{10}$ cm). This limits the total disc mass $M_{\text{disc}} \propto R_{\text{out}}^3$ which can build up in quiescence, so when the outburst is triggered and all this mass flows in on the viscous time-scale $t_{\text{visc}} \propto R_{\text{out}}$, then the mass accretion rate onto the central object is $M_{\text{disc}}/t_{\text{visc}} \propto R_{\text{out}}^2$ (King & Ritter 1998; Shahbaz, Charles & King 1998).

As the outburst declines there is a rather steep drop in the light-curve, after 26th of April (Fig. 1). This has been identified with the centrifugal barrier (Gilfanov et al. 1998). However, pulsed emission is *always* seen, so the magnetic field is not inhibiting accretion. Given that the system is transient we suggest instead that the drop is associated with the onset of the cooling wave, switching the disc back into quiescence (e.g. King & Ritter 1998; Dubus, Hameury & Lasota 2001).

4.6 Evolution of variance

The variance of the soft and hard components change in a rather different way as a function of time (see Fig. 9). The hard variance monotonically increases, while the soft variance follows the inner disc radius (assuming that this relates to the QPO frequency). If the disc is truncated by the magnetic field then the point at which the material connects on is the same as the inner disc radius. A larger disc radius means that the material connects onto field lines which are closer to the magnetic pole, so the projected area effects decrease, so the soft variance decreases (e.g. Frank, King & Raine 1992). This is exactly *opposite* to the observed behaviour (Figs. 9 and 10), strongly suggesting that the inner disc radius is truncated by some means other than that of the magnetic field. Since other atolls (and galactic black holes) show similar QPO behaviour then the mechanism must be an intrinsic property of the accretion flow.

If the optically thick disc truncates at some radius into an inner, optically thin flow (e.g. Różańska 1999; Meyer, Liu & Meyer-Hofmeister 2000), then the point at which this optically thin flow connects onto the magnetic field is deter-

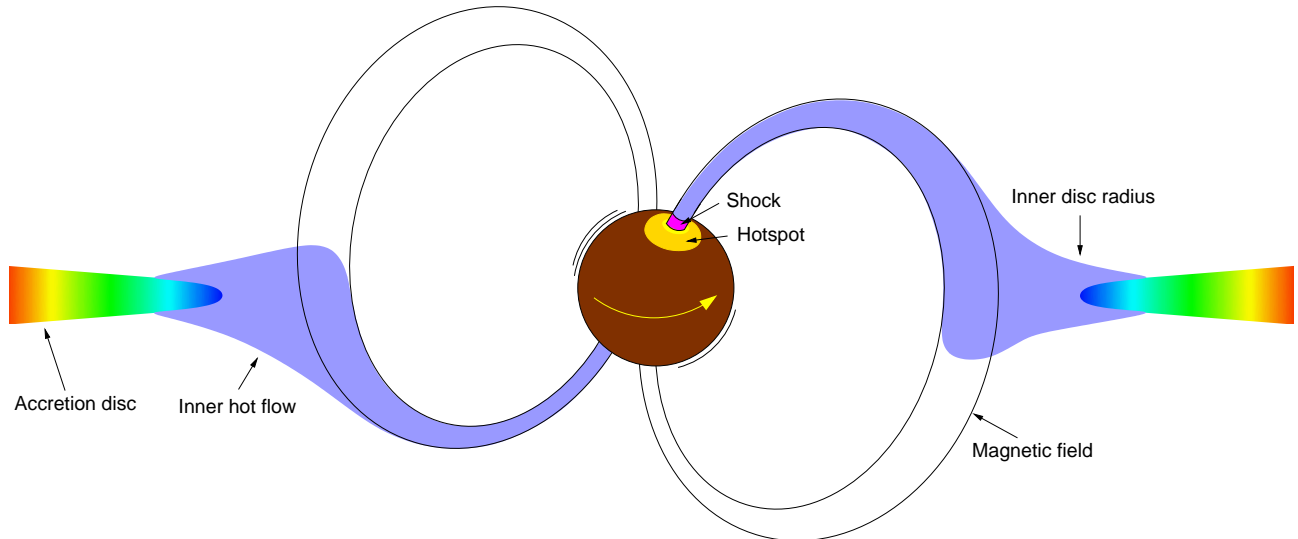


Figure 12. Sketch of the millisecond pulsar geometry. The accretion disc truncates at $\sim 20\text{--}40 R_g$ into an optically thin flow, which connects onto the magnetic field. The in-falling material creates a short shock – the source of hard X-ray emission. Further re-processing of the flow creates the hotspot on the surface, which feeds Comptonization in the shock with the seed photons.

mined by the ratio of its ram pressure to the magnetic pressure (e.g. Frank, King & Raine 1992). But if the inner disc retreat is connected with increased evaporation into the hot flow (Różańska 1999) then its density, and so its ram pressure, will be inversely related to the inner disc radius. As the inner edge of the optically thin disc recedes then the ram pressure of the hot flow increases so it penetrates further into the magnetosphere before connecting onto the field lines. The material then collimates onto a spot which is further from the magnetic pole, increasing the effective angle between the spot and the spin axis, so increasing the soft variability.

The hard component should then also increase its variance. However, as the mass accretion rate goes down, the shock optical depth probably decreases, while its height probably increases. The amount of variance apparently depends on the geometry and optical depth of the shock. In principle it is possible that these effects could contribute to the observed variance more than the position of the accretion column, and so explain the observed monotonic increase in variance.

4.7 Geometry

A geometry which is consistent with all the above constraints is one in which a neutron star with magnetic field $\sim 10^8$ G accretes from a disc which evaporates into an inner hot flow at some radius which is set by the overall evolution of the disc. This inner hot flow falls inward until its ram pressure is comparable with that of the magnetic field, after which point it is collimated by the field. It then free falls onto the magnetic poles, forming an accretion column (see Fig. 12).

All the other source properties are consistent with this geometry (see Appendices). The seed photons for Comptonization in the shock are probably from the surface of the neutron star, while the disc emission is negligible (Appendix A). Energy balance shows that these seed photons cannot

be only due to irradiation of the surface by the hard X-rays from the shock. Either reflection from the surface and/or re-processing of the kinetic energy of the in-falling material is necessary to support the sufficient amount of the seed photons (Appendix B). The reflection of the hard X-rays from the neutron star surface, though not detected, can be present in the data as a featureless cutoff power law (Appendix C). And finally, we applied one of the QPO models to the data and estimated the inner disc radius to vary between ~ 15 and $\sim 45 R_g$, consistent with the observed amount of the disc reflection (Appendix D).

4.8 The difference between SAX J1808.4–3658 and other atoll systems

We speculate that the true distinction between this and other LMXBs is purely an evolutionary effect. SAX J1808.4–3658 is highly evolved, the companion star is mostly evaporated/accreted. The mass transfer rate is very low, and has been low for a long time (King 2000). Models of accretion onto a magnetized neutron star suggest that the magnetic fields of up to $\sim 10^{11}$ G are buried by inflow where the accretion rate is a few per cent of Eddington. The field can diffuse back out, but only on time-scales of 100–1000 years (Cumming, Zweibel & Bildsten 2001). Only systems where the time averaged mass transfer rate has been lower than this for a few thousand years can have a magnetic field which is high enough to collimate the accretion flow.

5 CONCLUSIONS

We analyse spectra from SAX J1808.4–3658 from the whole *RXTE* campaign of 1998. This follows the April 1998 outburst as the luminosity declines by a factor of over 10. We fit physically motivated models to the phase-averaged spectrum from each observation, showing that the continuum

spectrum can be described by thermal Compton scattering of soft seed photons. This spectrum is reflected from the accretion disc, producing a weak reflected continuum and iron K α line as has been seen in other hard state (low mass accretion rate) LMXBs (Yoshida et al. 1993; Barret et al. 2000). However, there is also an additional component in the spectrum which can be fit by a blackbody. In phase-resolved spectroscopy it is this component which is most variable. The intensity of the soft component changes as the outburst progresses in the way expected for it to be produced by reprocessing of in-falling material energy on the neutron star surface. We show that the spectrum is consistent with a geometry where the disc is truncated at fairly large radii, the hard X-ray emission is from a shocked accretion column where the magnetically collimated flow impacts onto the neutron star surface, and the blackbody component is from the hotspot on the neutron star surface (see Fig. 12)

The disc cannot extend down to the last stable orbit as plainly the inner flow is collimated by the magnetic field. The truncation radius of the optically thick disc can be estimated by the QPO and break frequency seen in the variability power spectra assuming that these correspond to vertical perturbations at the inner disc edge (Psaltis & Norman 2001). The amount of reflection can also give an independent estimate for the inner disc edge. The two results are consistent, although the uncertainties are large, supporting the relativistic orbits interpretation of the QPOs. The inner radius evolution (as measured by the QPO frequency) is not at all consistent with the magnetic field truncating the disc. It seems much more likely that the accretion disc truncates spontaneously, and that the resulting inner hot accretion flow is then collimated by the magnetic field at rather smaller radii.

This has obvious application to other relativistic disc accreting systems, both neutron stars and black holes. These have very similar variability power spectra at low mass accretion rates to that of the millisecond pulsar. If the QPO/break frequency in the millisecond pulsar indicates the inner disc radius then it also shows that the disc is generally truncated in all the other disc accreting systems at low mass accretion rate. Given that we argue above that the disc in SAX J1808.4–3658 spontaneously truncates, then it seems likely that the same mechanism (whatever that is) operates generically in all low mass accretion rate discs.

Finally, we speculate that the reason SAX J1808.4–3658 is currently unique in showing spin pulsations is due to its evolutionary state. All the well known LMXB neutron star systems have a higher time averaged mass accretion rate which can bury the magnetic field below the surface.

6 SUMMARY

Summarizing the results from this paper, we find as follows:

- The X-ray spectrum of SAX J1808.4–3658 consists of the two components.
- The soft component is consistent with the blackbody. We find that most likely this emission originates from the hotspot on the neutron star surface, with radius ~ 4 km.
- The hard component is consistent with Comptonization of the seed photons from the hotspot in a plasma of intermediate optical depth and temperature of ~ 40 keV.

This is probably a short ($\lesssim 0.1R_*$) shock in the accretion column where the accreting material collimated by the magnetic field impacts onto the neutron star surface.

- The hard component includes also weak Compton reflection from the accretion disc. The amount of reflection implies that the disc is truncated at fairly large radii (20–40 R_g), consistent with the lack of relativistic smearing of the spectral features.
- Both components pulsate shifted in phase, while the neutron star rotates. This creates the energy-dependent time lags in which the soft photons lag the hard ones.
- The inner disc radius derived from the break and QPO frequencies is consistent with the inner disc radius derived from the solid angle subtended by the reflected spectrum. It evolves independently of the instantaneous accretion rate, implying that the inner disc radius is independent of and larger than the magnetospheric radius. The magnetic field does not truncate the disc in SAX J1808.4–3658. Instead, the inner disc radius is set by some much longer time-scale process, most probably connected to the overall evolution of the accretion disc.
- The disc truncation mechanism is probably generic to low mass accretion rate flows both in disc accreting neutron stars and black hole systems.
- We do not detect Compton reflection from the neutron star surface, though we predict that it should be present in the X-ray spectrum. This would give an unambiguous observational measure of M/R if there is any iron on the neutron star surface which is not completely ionized.

ACKNOWLEDGEMENTS

This research has been supported in part by the Polish KBN grants 2P03D00514, 2P03D00614, by the Foundation for Polish Science fellowship 15,4/99 and by a Polish-French exchange program.

REFERENCES

Arnaud K. A., 1996, in Jacoby G. H., Barnes J., eds., Astronomical Data Analysis Software and Systems V. ASP Conf. Series Vol. 101, San Francisco, p. 17

Barret D., Olive J. F., Boirin L., Done C., Skinner G. K., Grindlay J. E., 2000, ApJ, 533, 329

Bhattacharya D., Srinivasan G., 1995, in Lewin W. H. G., van Paradijs J., van den Heuvel E. P. J., eds., X-ray Binaries, Cambridge University Press, Cambridge, p. 495

Bildsten L., Chakrabarty D., 2001, astro-ph/0104153

Chakrabarty D., Morgan E. H., 1998, Nature, 394, 346

Chandler A. M., Rutledge R. E., 2000, ApJ, 545, 1000

Churazov E., Gilfanov M., Revnivtsev M., 2001, MNRAS, 321, 759

Cook G. B., Shapiro S. L., Teukolsky S., 1994, ApJ, 424, 823

Cui W., Morgan E. H., Titarchuk L. G., 1998, ApJ, 504, L27

Cumming A., Zweibel E. G., Bildsten L., 2001, astro-ph/0102178

Dubus G., Hameury J.-M., Lasota J.-P., 2001, A&A, 373, 251

Ergma E., Antipova J., 1999, A&A, 343, 45L

Friedman J. L., Ipser J. R., Parker L., 1986, ApJ, 304, 115

Ford E. C., 2000, ApJ, 535, L119

Ford E. C., van der Klis M., Méndez M., Wijnands R., Homan J., Jonker P. G., van Paradijs J., 2000, ApJ, 537, 368

Frank J., King A., Raine D., 1992, Accretion Power in Astrophysics, Cambridge University Press, Cambridge

Friedman J. L., Parker L., Ipser J. R., 1986, ApJ, 304, 115
 George I. M., Fabian A. C., 1991, MNRAS, 249, 352
 Gilfanov M., Revnivtsev M., Sunayev R., Churazov E., 1998, A&A, 338, 83
 Hasinger G., van der Klis M., 1989, A&A, 225, 79
 Heindl W. A., Smith D. M., 1998, ApJ, 506, 35
 in 't Zand J. J. M., Heise J., Muller J. M., Bazzano A., Cocchi M., Natalucci L., Ubertini P., 1998, A&A, 331, L25
 in 't Zand J. J. M., et al., 2001, astro-ph/0104285
 King A. R., 2000, MNRAS, 315, L33
 King A. R., Ritter H., 1998, MNRAS, 293, L42
 Kompaneets A. S., 1956, Soviet Phys., JETP 31, 876
 Magdziarz P., Zdziarski A. A., 1995, MNRAS, 273, 837
 Meyer F., Liu B. F., Meyer-Hofmeister E., 2000, A&A, 361, 175
 Méndez M., van der Klis M., Ford E. C., Wijnands R., van Paradijs J., 1999, ApJ, 511, L49
 Miller M. C., Lamb F. K., Psaltis D., 1998, ApJ, 508, 791
 Mitsuda K., Inoue H., Nakamura N., Tanaka Y., 1989, PASJ, 41, 97
 Morrison R., McCammon D., 1983, ApJ, 270, 119
 Nowak M. A., 1995, PASP, 107, 1207
 Poutanen J., Svensson R., 1996, ApJ, 470, 249
 Psaltis D., Chakrabarty D., 1999, ApJ, 521, 332
 Psaltis D., Norman C., 2001, astro-ph/0001391
 Psaltis D., Özel F., DeDeo S., 2000, ApJ, 544, 390
 Różańska A., 1999, MNRAS, 308, 751
 Ruderman M., 1991, ApJ, 366, 261
 Shahbaz T., Charles P. A., King A. R., 1998, MNRAS, 301, 382
 Stella L., Vietri M., 1998, ApJ, 492, L59
 van der Klis M., 1995, in Lewin W. H. G., van Paradijs J., van den Heuvel E. P. J., eds., X-ray Binaries, Cambridge University Press, Cambridge, P. 252
 Vaughan B. A., et al., 1994, ApJ, 435, 362
 Wardziński G., Zdziarski A. A., 2000, MNRAS, 314, 183
 Wijnands R., van der Klis M., 1998a, Nature, 394, 344
 Wijnands R., van der Klis M., 1998b, ApJ, 507, L63
 Wijnands R., van der Klis M., 1999, ApJ, 514, 939
 Wijnands R., Méndez M., Markwardt C., van der Klis M., Chakrabarty D., Morgan E., 2001, astro-ph/0105446
 Wilson C. D., Done C., 2001, MNRAS, 325, 167
 Yoshida K., Mitsuda K., Ebisawa K., Ueda Y., Fujimoto R., Yaqoob T., Done C., 1993, PASJ, 45, 605
 Zdziarski A. A., Johnson W. N., Magdziarz P., 1996, MNRAS, 283, 193
 Życki P., Done C., Smith D. A., 1998, ApJ, 496, L25

APPENDIX A: SEED PHOTONS

Here we quickly discuss the possible sources of the seed photons for Comptonization. Let us consider a Comptonizing region elevated at height h above the pole of the neutron star of radius R_* . It can receive the seed photons from the accretion disc and from the hotspot on the surface. We consider the Shakura-Sunyaev disc extending from R_{in} to infinity, around the neutron star of mass M and with accretion rate \dot{M} . The circular hotspot of radius R_{spot} and temperature T_{spot} is located on the spin pole (for these estimations only). We assume $M = 1.4M_{\odot}$ and $\dot{M} = 5 \times 10^{16} \text{ g s}^{-1}$.

The energy density of the photons from the disc in the Comptonizing region is

$$u_{\text{disc}} = \frac{3GMM}{4c\pi(R_* + h)^3} \left[\frac{X}{R_{\text{in}}} + \frac{R_{\text{in}}}{X} - 2 \right], \quad (\text{A1})$$

where $X = [(R_* + h)^2 + R_{\text{in}}^2]^{1/2}$. The energy density of the photons from the hotspot in the Comptonizing region is

$$u_{\text{spot}} = \frac{2\sigma T_{\text{spot}}^4}{c} \left[1 - \frac{h}{(h^2 + R_{\text{spot}}^2)^{1/2}} \right]. \quad (\text{A2})$$

For a short shock, $h = 0.1R_*$, the hotspot of radius $0.4R_*$ and the inner disc radius of $30R_g$, $u_{\text{spot}}/u_{\text{disc}} \approx 900$. The two quantities are comparable only if the shock is tall ($h \gtrsim 2R_*$), which we find unlikely (see Section 4.3).

The energy density of the self-absorbed synchrotron seed photons in plasma of temperature $\theta \equiv kT_e/m_ec^2$ and magnetic field $B = B_8 10^8 \text{ G}$ is

$$u_{\text{magn}} = \frac{8\pi\nu_t^3}{3c^3} kT_e, \quad (\text{A3})$$

where $\nu_t \approx 9.8 \times 10^{16} \theta^{0.95} \tau^{0.05} B_8^{0.91} \text{ Hz}$ is the turnover frequency (Wardziński & Zdziarski 2000). For $\theta = 0.1$, $\tau = 1$ and $B = 10^8 \text{ G}$ we find $u_{\text{spot}}/u_{\text{magn}} \approx 400$. Therefore, we conclude that the dominating source of the seed photons for Comptonization is the hotspot on the neutron star surface, which is at the same time a source of the soft component (blackbody) seen in the X-ray spectrum.

APPENDIX B: ENERGY BALANCE

Let us consider a source of the hard component located above the neutron star surface and irradiating it. A fraction of the irradiating luminosity is then re-processed and re-emitted as seed photons for Comptonization. Here we check whether our assumed geometry is consistent with the energy balance in such a Comptonizing closed cycle.

The luminosity of the hard component is L_{hard} . A fraction $d \times \Omega_*/2\pi$ of it is intercepted by the surface, where Ω_* is the solid angle subtended by the surface to the hard X-ray source, and d accounts for intrinsic anisotropy of Comptonization. The surface has albedo A , so the power in the re-processed photons is $L_{\text{irr}} = d(1 - A)(\Omega_*/2\pi)L_{\text{hard}}$. On the other hand the Comptonizing cloud amplifies the seed photons, giving rise to the hard component luminosity, $L_{\text{hard}} = C(\Omega_X/2\pi)L_{\text{seed}}$, where Ω_X is the solid angle subtended by the hard X-ray source to the hotspot and C is Compton amplification factor. Hence,

$$\frac{L_{\text{irr}}}{L_{\text{seed}}} = dC(1 - A) \frac{\Omega_X}{2\pi} \frac{\Omega_*}{2\pi}. \quad (\text{B1})$$

The maximum albedo here is $A \sim 0.8$ because the hard $\geq 30 \text{ keV}$ photons are Compton down-scattered and cannot be completely reflected. However, there is also a minimum albedo of $A \sim 0.7$ since the observed temperature is $\sim 0.5\text{--}0.7 \text{ keV}$, and so the material is probably highly ionized from collisional ionization.

We have performed Monte Carlo simulations of the observed spectrum and found $d = 0.57$ and $C = 3.6$ (in the slab geometry). Then, the photons re-processed from irradiation can account only for about $0.4(\Omega_X/2\pi)(\Omega_*/2\pi)$ of the seed photons. Both solid angles are less than 2π (though not much less for a short shock), so 0.4 constitutes a firm upper limit on $L_{\text{irr}}/L_{\text{seed}}$. Therefore, there must be an additional source of the seed photons. Since they must come from the neutron star surface (Appendix A), we suggest the following two possibilities.

First, the additional seed photons can originate from reflection from the neutron star surface (see Appendix C). Due

to large albedo the luminosity carried by the photons Compton reflected from the surface is roughly four times luminosity in the re-processed photons. Second, the in-falling material kinetic energy can be directly re-processed into heating of the hotspot, additionally to the irradiation, and this process can give rise to the blackbody seed photons.

We note that an anisotropy of the hard X-ray source (e.g. due to bulk motion Comptonization) cannot boost the re-processed emission enough to reach the equilibrium. Even if all of the hard X-ray luminosity was directed towards the neutron star ($d = 1$), then $L_{\text{irr}}/L_{\text{seed}}$ would be still significantly less than 1.

APPENDIX C: REFLECTION FROM THE NEUTRON STAR SURFACE

In Section 3.2 we have derived an upper limit on the reflection from a mildly ionized star, $\Omega_*/2\pi < 0.012$. Such a small solid angle subtended by the star would require an irradiating source at a distance $\sim 10R_*$ from the surface, implying a *very tall* shock, which we find unlikely. A more likely short shock of $H_{\text{shock}} = 0.1R_*$ subtends an angle $\Omega_*/2\pi = 0.6$. This can be in agreement with the observations only if the reflected spectrum is featureless, which means that either the reflecting spectrum is completely ionized or the heavy elements, including iron, sank under the surface in the strong gravitational field, so the surface could act as a mirror. The component reflected from the surface would then contribute to the total spectrum as a power-law of the same index as the irradiating Comptonization and a high-energy cutoff above ~ 30 keV. Such a component would be impossible to disentangle from the Comptonization in *RXTE* data.

APPENDIX D: ACCRETION DISC GEOMETRY

Here we consider a particular QPO model and check whether the results obtained from it are consistent with the our assumed geometry of SAX J1808.4–3658. If the (low frequency) QPO is connected to the precession time-scale of a vertical perturbation in the disc (Stella & Vietri 1998; Psaltis & Norman 2001) then its frequency is uniquely linked to some transition radius (we assume it is the inner radius $r_{\text{in}} \equiv R_{\text{in}}/R_g$) in the disc, as (Psaltis & Norman 2001)

$$\nu_{\text{QPO}} \approx 2 \times 10^5 \frac{1}{mr_{\text{in}}^{3/2}} \frac{1 - \sqrt{1 - 4a_*r_{\text{in}}^{-3/2}}}{\sqrt{1 + a_*r_{\text{in}}^{-3/2}}} \text{ Hz}, \quad (\text{D1})$$

where $m \equiv M_*/M_{\odot}$ is the mass and $a_* \equiv Jc/GM^2$ is the spin on the neutron star. All current equations of state yield $0.1 < a_* < 0.4$ (Friedman, Parker & Ipser 1986; Cook, Shapiro & Teukolsky 1994), and we assume $m = 1.4$.

Since we do not observe the QPO in all of our observations, we use the empirical relation between the break and QPO frequencies from the fit to the data,

$$\nu_{\text{break}} = 0.10 \nu_{\text{QPO}}^{1.10} \text{ Hz}, \quad (\text{D2})$$

to estimate all the QPO frequencies. This, together with equation (D1) implies the inner disc radius varying between $17\text{--}29R_g$ ($a_* = 0.1$) or $26\text{--}45R_g$ ($a_* = 0.4$). These rather large radii are consistent with the rather small amount of

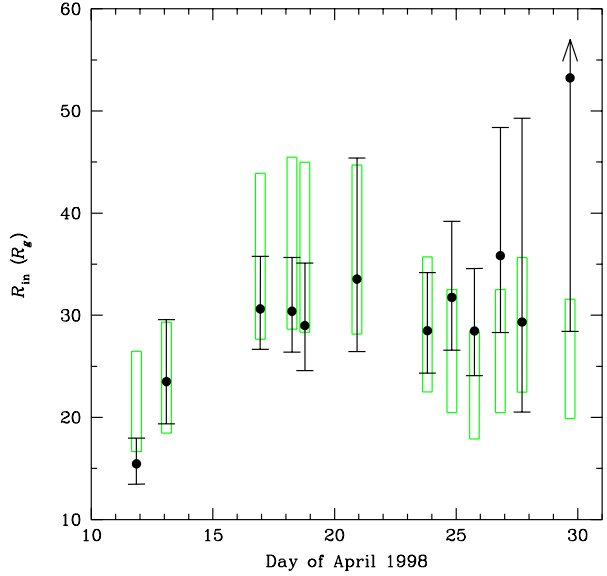


Figure D1. The inner disc radius. Squares indicate the inner radius range for $0.1 < a_* < 0.4$, predicted from the fast variability (Equation D1). Filled circles (with error bars) show the inner disc radius derived from the observed amplitude of reflection (see Fig. 3), assuming that a half of the disc is irradiated by the shock just above the neutron star surface.

relativistic smearing of the reflected spectral features which require that the disc is always larger than $20R_g$ (see Section 3.2).

The solid angle subtended by the disc as measured by the reflected spectrum gives us an independent way to estimate the inner disc radius. The hard X-ray emission can only illuminate half the disc in our geometry where most of the hard X-ray emission comes from a short shock above the magnetic pole. Then we derive the inner disc radius as shown in Fig. D1, which is consistent with the radii derived from the QPO frequencies.

The behaviour of the inner disc radius is rather complex. It evolves on the long time-scale of days. It first recedes as the outburst declines, then comes in again and then recedes (Fig. D1), rather than being uniquely related to the instantaneous mass accretion rate onto the compact object. This lack of correlation with the mass accretion rate is generally seen in other LMXBs, e.g. 4U 1608–52 (Méndez et al. 1999), showing that the key determinant of the behaviour of the system is tied instead to something with a longer time-scale, most probably the overall evolution of the disc.